

Analysis and experiment of capillary valves for microfluidics on a rotating disk

Jerry M. Chen · Po-Chun Huang · Mou-Gee Lin

Received: 20 April 2007 / Accepted: 27 June 2007 / Published online: 27 July 2007
© Springer-Verlag 2007

Abstract This paper presents an analytical expression of the pressure barrier in a capillary-burst valve for flow regulation in centrifugal microfluidics. The analysis considers variations of the interfacial energies at the meniscus of three-dimensional (3D) configuration in a rectangular microchannel with a sudden expansion in cross-section. We derive a simple expression that predicts the critical burst pressure or rotational speed to overcome the capillary valve. Experiments were carried out for capillary valves that were integrated with microchannels on a rotating disk having various cross-sectional dimensions (300 and 400 μm in width and 80–600 μm in depth) and wedge angles (30°–100°) of sudden expansion. The flow visualization of the meniscus development across the capillary valve supports the assumptions made for the present analysis. The measurements of burst rotational speeds for the capillary valves are in good agreement with the predictions by the simple expression except that those with a larger channel width and wider wedge angles are nearly 10% lower than the predicted values.

Keywords Capillary valve · Rectangular microchannel · Burst pressure · Centrifugal microfluidics

1 Introduction

Integrated microfluidic systems have received rapidly increasing attention over the past decade for their novel

applications in analysis or synthesis for chemistry and biology (Manz et al. 1990; Reyes et al. 2002; Auroux et al. 2002; Nguyen and Wereley 2002). In these microfluidic systems, the capability of precisely controlling fluid flow of small amount is essential. The large surface-to-volume ratio in microfluidics makes it possible to control microfluidic flow through the use of capillary forces as a valve. Unlike the conventional diaphragm valves, capillary valving requires no moving parts (Oh and Ahn 2006).

Capillary valves may be designed actively utilizing different effects such as electrocapillary and thermocapillary (Marangoni) to change surface tensions of the meniscus (Lee et al. 2002; Nguyen and Huang 2005). More often, they are designed passively as a check-valve simply by making an abrupt change of geometry in the hydrophobic or hydrophilic microchannels (McNeely et al. 1999; Duffy et al. 1999) and the trigger of flow can be achieved by centrifugal force or other forces like electrics and pressure. Passive capillary valves have been frequently used to regulate liquid flow in the compact disk (CD)-based centrifugal microfluidics to which the ease of implementing valves is vitally important (Madou et al. 2001a,b). Centrifugal microfluidics has been demonstrated to provide promising platforms for efficient mixing and high-throughput screening, while its applications to sensing and diagnostic tests require more severe technical challenges (Gustafsson et al. 2004; Grumann et al. 2005; Haeberle et al. 2006; Madou et al. 2006). In this study we present the analysis of three-dimensional (3D) model along with the experiments on capillary-burst valves for regulation of microfluidic flow on a rotating disk.

Figure 1 shows the schematic configuration of the CD-based hydrophilic microfluidics where the capillary-burst valve is connected to a reservoir near the rotational center through a straight microchannel. When the disk is at

J. M. Chen (✉) · P.-C. Huang · M.-G. Lin
Department of Mechanical Engineering,
National Chung Hsing University,
Taichung 402, Taiwan
e-mail: jerry@dragon.nchu.edu.tw

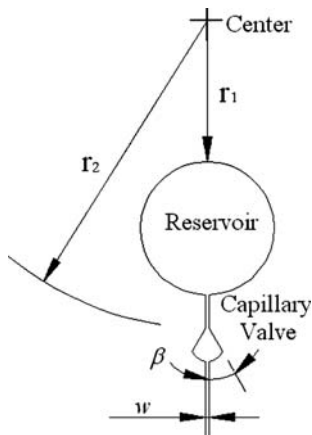


Fig. 1 Schematic of microfluidics fabricated on a rotating disk equipped with a capillary valve to regulate the centrifugal-driven flow. A straight microchannel links the reservoir and the capillary valve

rest, the liquid stored in the reservoir flows to fill the hydrophilic channel but stops at the inlet to the suddenly expanded valve due to the capillary force (barrier pressure) created on the liquid front in the direction towards the center. As the disk is rotating the centrifugal force induces a pressure at the liquid front opposite to the barrier pressure. The centrifugally induced pressure Δp_c , that is in the form of artificial gravity acting on fluid volume, for the resting liquid plug simply yields

$$\Delta p_c = \rho \Omega^2 \Delta r r_m \quad (1)$$

where ρ is the liquid density, Ω is the angular frequency, $\Delta r = r_2 - r_1$ is the length of the liquid plug with its fronts located r_1 in the reservoir and r_2 in the capillary-burst valve from the rotational center, and $r_m = (r_2 + r_1)/2$. When the rotational speed of the disk exceeds a threshold value, the centrifugal force becomes larger than the capillary force causing the liquid to burst into the expanded volume of the valve. Capillary valves can be designed with different wedge angles β associated with the channel dimensions to create different barrier pressures. It is important to calculate these two forces for manipulating the rotational microfluidic flow.

Despite the simple expression of the centrifugally induced pressure, the barrier pressure on the other hand can be extremely complicated depending on the capillary valve geometry and the liquid–air–solid interfacial properties. For capillary valves with axisymmetric cross-sections and a sudden opening of $\beta = 90^\circ$, the maximum barrier pressure at the liquid front termed the burst pressure Δp_b is given by (Zeng et al. 2000)

$$\Delta p_b = 4\gamma_{la} \sin \theta_c / D_h \quad (2)$$

where γ_{la} is the liquid–air surface tension, θ_c is the contact angle, and D_h is the hydraulic diameter of the channel. This

1D theory of Eq. 2 may suffer significant error when the microchannel geometry deviates largely from the assumed circular shape. Duffy et al. (1999) modified the 1D theory to obtain an expression of the form

$$\Delta p_b = a(4\gamma_{la}/D_h) + b \quad (3)$$

with two empirical constants, a accounting for variation of channel cross-section and b representing the pressure required to wet the expanded volume beyond the valve. The term b depends on the geometry of the volume to be filled and the wettability of its walls. Man et al. (1998) derived a 2D theory for the barrier pressure developed in the capillary valve from the energy changes in the liquid–air–solid interface system. However, the 2D theory that was derived assuming large aspect (depth-to-width) ratio of the channel cross-section may not be valid for channels having an aspect ratio near unity or smaller. Numerical simulations of 3D multiphase flow to compute the barrier pressure have been carried out by Zeng et al. (2000) based on a Navier–Stokes solver coupled with the volume of fluids method. The 3D multiphase flow simulations often require considerable computational time. Glière and Delattre (2006) later approached the 3D simulations by solving the static momentum equations for the equilibrium free surface. However, the numerical solutions for this simpler approach could still become complicated and challenging dependent on the geometric parameters chosen for the surface profile.

An analytical expression of the barrier pressure based on a 3D configuration should be greatly helpful for design and fabrication of the capillary-burst microfluidic valves. The analysis would also offer a more transparent, in-depth understanding of the physics occurring in the capillary valve. Leu and Chang (2004) recently reported the analysis of pressure barrier based on the model of 3D meniscus. However, the magnitude of burst pressure obtained in their Fig. 6 is shown to decrease with increasing aspect ratio (A_R) for $A_R > 1$ appearing to be inconsistent with the 2D results of Man et al. (1998). This decreasing trend of burst pressure with aspect ratio in the large range will also be shown opposite to the measurements of the present study. Cho et al. (2007) most recently explained the working principle of a capillary-burst valve based on the theory of contact line movement in a circular channel meeting a suddenly expanded section and obtained the burst condition of the valves in both circular and rectangular channels. Nevertheless, a more rigorous analysis based on a 3D structure is still desired to clarify the fundamental mechanism of a capillary-burst valve.

In the following sections, we first present the 3D modeling and analysis of the capillary-burst microfluidic valves for rectangular transport channels with various aspect

ratios. The analytical expression of burst pressure derived from the 3D model is compared with the results of aforementioned 1D and 2D theories. Then we describe the experimental apparatus developed for visualization and measurements of the liquid flow in the rotating microfluidics. The visualization experiments provide sequential images of the microfluidic flow. The measurements of burst rotational speeds for the capillary valves are used to verify the analytical results.

2 Analysis of capillary valve

2.1 Pressure barrier

Figure 2 illustrates the 3D configuration of liquid injected into a microchannel with a sudden opening. The channel has a constant cross-section of h (depth) \times w (width) from an arbitrarily axial position $x_c = 0$ to L and then is followed by a divergent section with a wedge angle β in the width direction while the depth remains unchanged throughout the entire channel. In the present 3D model, the meniscus is assumed to have two circular arcs in both the width and depth directions with angles of $2\alpha_w$ and $2\alpha_h$, respectively. The thermodynamics in terms of interfacial free energy may be applied to obtain the pressure barrier (Kim and Whitesides 1997; Man et al. 1998) for the solid–liquid–air system. The total interfacial energy U_T of the solid–liquid–air system is given by

$$U_T = A_{sl}\gamma_{sl} + A_{sa}\gamma_{sa} + A_{la}\gamma_{la} \quad (4)$$

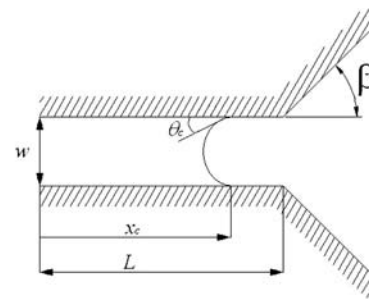
where A_{sl} , A_{sa} and A_{la} are solid–liquid, solid–air and liquid–air interface areas, and γ_{sl} and γ_{sa} denote the solid–liquid and solid–air surface tensions (surface energy per unit area), respectively. After the use of Young's equation, which relates the contact angle to the surface tensions involved, the total energy becomes

$$U_T = U_0 - A_{sl}\gamma_{la} \cos \theta_c + A_{la}\gamma_{la} \quad (5)$$

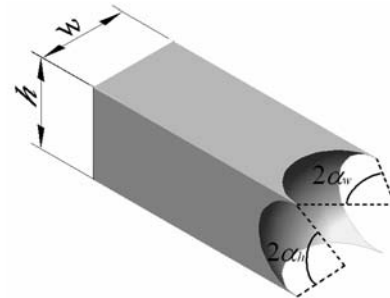
where θ_c is the equilibrium contact angle and $U_0 = \gamma_{la}(A_{sl} + A_{sa})$ represents the constant energy component due to constant sum of the solid–liquid and solid–air interfaces. The pressure p in the liquid can be derived from the change of total interfacial energy of the solid–liquid–air system with respect to the injected liquid volume V_l as

$$p = -\frac{dU_T}{dV_l} = \gamma_{la} \left(\cos \theta_c \frac{dA_{sl}}{dV_l} - \frac{dA_{la}}{dV_l} \right) \quad (6)$$

where only the liquid–air surface tension and solid–liquid and liquid–air interface areas are involved.



(a) Top view of the capillary-burst valve.



(b) 3D shape of a liquid plug and meniscus in a rectangular channel.

Fig. 2 Schematic configuration and parameters defined for the meniscus developed in a rectangular capillary channel. Only part of the straight channel in Fig. 1 is shown here. The straight channel starts from an arbitrarily position $x_c = 0$ and ends at the valve edge $x_c = L$

The pressure in the liquid may also be determined using the Laplace equation

$$p = \gamma_{la} \left(\frac{1}{R_w} + \frac{1}{R_h} \right) \quad (7)$$

where R_w and R_h are the principal radii of curvature of the meniscus in the width and height directions. In fact, it is easier to obtain the liquid pressure using Eq. 7 than Eq. 6 for the straight microchannel regime ($x_c < L$). By substituting the geometric relations

$$R_w = \frac{w}{2 \cos \theta_c} \text{ and } R_h = \frac{h}{2 \cos \theta_c} \quad (8)$$

into Eq. 7, we arrive at the Young–Laplace equation of the form (Kim et al. 2002)

$$p = 2\gamma_{la} \cos \theta_c \left(\frac{1}{w} + \frac{1}{h} \right) \quad (9)$$

The above equation indicates that a positive, constant pressure propels the liquid originated from an arbitrary position $x_c = 0$ toward the sudden opening at the end of the straight microchannel. This positive, constant pressure can be realized from Eq. 6. As the liquid floods the uniform

channel of hydrophilic surface ($\theta_c < 90^\circ$), A_{la} is fixed and A_{sl} increases linearly with the liquid volume V_l . The liquid maintains constant pressure until its front reaches the intersection of the sudden opening ($x_c = L$), referred to as the transition regime.

In the transition regime, the solid–liquid–air contact line is fixed at $x_c = L$ where the cross section of the channel is discontinuous and an increase in the liquid volume requires meniscus curvature to reduce through both the angles α_w and α_h . The total interfacial energy U_T in this regime can be expressed as

$$U_T = U_0 - 2\gamma_{la} \cos \theta_c \left[(h+w)L - \frac{w^2}{4 \sin \alpha_w} \left(\frac{\alpha_w}{\sin \alpha_w} - \cos \alpha_w \right) - \frac{h^2}{4 \sin \alpha_h} \left(\frac{\alpha_h}{\sin \alpha_h} - \cos \alpha_h \right) \right] + \gamma_{la} \left(\frac{hw\alpha_w\alpha_h}{\sin \alpha_w \sin \alpha_h} \right) \quad (10)$$

where $\pi/2 - \theta_c > \alpha_w \geq \pi/2 - \theta_c - \beta$ and $\pi/2 - \theta_c > \alpha_h \geq 0$, the second term on the right represents the energy contribution from solid–liquid interface, and the last term represents the energy from the liquid–air interface. The liquid volume is approximated as (Leu and Chang 2004)

$$V_l = hwL - \frac{hw^2}{4 \sin \alpha_w} \left(\frac{\alpha_w}{\sin \alpha_w} - \cos \alpha_w \right) - \frac{h^2w\alpha_w}{4 \sin \alpha_h \sin \alpha_w} \left(\frac{\alpha_h}{\sin \alpha_h} - \cos \alpha_h \right) \quad (11)$$

It should be noted that the variation of meniscus profile in this regime may be divided into two stages based on the changes in α_w and α_h . In the first stage, both α_w and α_h vary from a positive value to zero ($\pi/2 - \theta_c > \alpha_w \geq 0$ and $\pi/2 - \theta_c > \alpha_h \geq 0$), that is from a concave meniscus to a flat one. If the wedge angle is large enough, the meniscus will develop into the second stage, resulting in a convex meniscus to reconcile the wedge angles along the width direction. When applying Eq. 6 to obtain the pressure in this regime, we need an additional constraint imposing on the meniscus curvatures in the form

$$f(\alpha_w, \alpha_h) = 0 \quad (12)$$

The constraint governs the “trajectory” of meniscus growth in the first stage. For a rectangular channel made of the same material, it is reasonable to assume the constraint of $\alpha_w - \alpha_h = 0$, which means an equal variation in α_w and α_h . For the channel constructed using different materials, the equal variation constraint may be no longer valid and one should consider a more complex relation between α_w and α_h . With a known constraint on the meniscus curvatures, the pressure in the first stage yields

$$p = -\frac{dU_T}{dV_l} = -\frac{\left(\frac{\partial U_T}{\partial \alpha_w}\right) + \left(\frac{\partial U_T}{\partial \alpha_h}\right) \left[-\frac{\partial f}{\partial \alpha_w} \left(\frac{\partial f}{\partial \alpha_h}\right)^{-1}\right]}{\left(\frac{\partial V_l}{\partial \alpha_w}\right) + \left(\frac{\partial V_l}{\partial \alpha_h}\right) \left[-\frac{\partial f}{\partial \alpha_w} \left(\frac{\partial f}{\partial \alpha_h}\right)^{-1}\right]} \quad (13)$$

where

$$\frac{\partial U_T}{\partial \alpha_w} = \gamma_{la} \left(\frac{w^2 \cos \theta_c}{\sin \alpha_w} + \frac{hw\alpha_h}{\sin \alpha_h} \right) \left(\frac{\sin \alpha_w - \alpha_w \cos \alpha_w}{\sin^2 \alpha_w} \right), \quad (14a)$$

$$\frac{\partial U_T}{\partial \alpha_h} = \gamma_{la} \left(\frac{h^2 \cos \theta_c}{\sin \alpha_h} + \frac{hw\alpha_w}{\sin \alpha_w} \right) \left(\frac{\sin \alpha_h - \alpha_h \cos \alpha_h}{\sin^2 \alpha_h} \right), \quad (14b)$$

$$\frac{\partial V_l}{\partial \alpha_w} = -\left[\frac{hw^2}{2 \sin \alpha_w} + \frac{h^2w}{4 \sin \alpha_h} \left(\frac{\alpha_h}{\sin \alpha_h} - \cos \alpha_h \right) \right] \times \left(\frac{\sin \alpha_w - \alpha_w \cos \alpha_w}{\sin^2 \alpha_w} \right), \quad (14c)$$

$$\frac{\partial V_l}{\partial \alpha_h} = -\frac{h^2w\alpha_w}{2 \sin \alpha_h \sin \alpha_w} \left(\frac{\sin \alpha_h - \alpha_h \cos \alpha_h}{\sin^2 \alpha_h} \right) \quad (14d)$$

In the second stage, it is assumed that only α_w continues to change from zero to negative ($0 > \alpha_w \geq \pi/2 - \theta_c - \beta$) while α_h remains unchanged holding at $\alpha_h = 0$. The change in α_w brings the “effective” contact angle $\theta_{\text{eff}} = \pi/2 - \alpha_w$ β in the width direction to approach the equilibrium contact angle θ_c until the burst of the liquid into the expanded volume. The pressure in this stage can be derived as

$$p = -\left(\frac{\partial U_T}{\partial \alpha_w}\right) \left(\frac{\partial V_l}{\partial \alpha_w}\right)^{-1}_{\alpha_h=0} = -\left\{ \gamma_{la} \frac{w^2 \cos \theta_c}{\sin \alpha_w} \left(\frac{\sin \alpha_w - \alpha_w \cos \alpha_w}{\sin^2 \alpha_w} \right) + \gamma_{la} \frac{hw\alpha_h}{\sin \alpha_h} \left(\frac{\sin \alpha_w - \alpha_w \cos \alpha_w}{\sin^2 \alpha_w} \right) \right\} \left\{ -\frac{hw^2}{2 \sin \alpha_w} \left(\frac{\sin \alpha_w - \alpha_w \cos \alpha_w}{\sin^2 \alpha_w} \right) \right\}^{-1} \quad (15)$$

$$= \frac{2\gamma_{la}}{w} \left[\left(\frac{w}{h}\right) \cos \theta_c + \sin \alpha_w \right]$$

Note that the term $\alpha_h/\sin \alpha_h$ in the above expression is taken to be unity as $\alpha_h \rightarrow 0$. Moreover, the pressure in this stage turns negative as the meniscus curvature α_w becomes large enough in the negative sense, i.e. $\sin(-\alpha_w) > (w/h)\cos \theta_c$.

In the third regime ($x_c > L$), the liquid expands into the divergent section of the channel. The total free energy in the expansion regime is expressed as

$$U_T = U_0 - 2\gamma_{la} \cos \theta_c$$

$$\times \left[L(h+w) + x_{cL} \left(\frac{h}{\cos \beta} + w + x_{cL} \tan \beta \right) \right]$$

$$\times \left[-\frac{(w+2x_{cL} \tan \beta)^2}{4 \sin \alpha_w} \left(\frac{\alpha_w}{\sin \alpha_w} - \cos \alpha_w \right) \right]$$

$$\times \left[-\frac{h^2}{4 \sin \alpha_h} \left(\frac{\alpha_h}{\sin \alpha_h} - \cos \alpha_h \right) \right]$$

$$+ \gamma_{la} \left[(w+2x_{cL} \tan \beta) \frac{h\alpha_w\alpha_h}{\sin \alpha_w \sin \alpha_h} \right]$$
(16)

where $x_{cL} = x_c - L$ denotes the horizontal position of the liquid–solid–air interface in the divergent section. The liquid volume is approximated as

$$V_l = h[wL + wx_{cL} + x_{cL}^2 \tan \beta]$$

$$- \frac{(w+2x_{cL} \tan \beta)^2}{4 \sin \alpha_w} \left(\frac{\alpha_w}{\sin \alpha_w} - \cos \alpha_w \right)$$

$$- \frac{h^2}{4 \sin \alpha_h} \left(\frac{\alpha_h}{\sin \alpha_h} - \cos \alpha_h \right) \left[(w+2x_{cL} \tan \beta) \frac{\alpha_w}{\sin \alpha_w} \right]$$
(17)

The liquid pressure can be obtained again from Eq. 6 as

Here only the change in x_{cL} is considered for the variations of U_T and V_l while the curvatures α_w and α_h of the meniscus are assumed to be unchanging (Man et al. 1998). The pressure derived in this regime is more complex depending on the geometry of the divergent section as well as the wetted length in this section.

The pressure of the liquid in a 3D microchannel with sudden expansion as depicted in Fig. 2 can be computed from Eqs. 9, 13, 15 and 18 for the corresponding regimes. Figure 3 illustrates the pressure of the liquid as a function of the liquid volume for a square channel with a wedge angle in the width direction ranging from $\beta = 0^\circ$ – 100° . Note that the constraint of $\alpha_w - \alpha_h = 0$ is used in Eq. 13 to compute the pressure. In the straight channel regime, the constant positive pressure of 0.360 kPa drives the wicking until the meniscus reaches the valve edge entering the transition regime. In the transition regime, the pressure falls rapidly from the positive constant value. For small β the pressure due to interfacial tension is still in the positive range. This means that the capillary force propels the liquid forward across the valve, which is a “valveless” condition. As $\beta \geq 50^\circ$, the pressure tends to further decrease to reach a negative and then rises gradually. In this situation, the flow is blocked by the valve and its magnitude of negative pressure (pressure barrier) varies with the geometry of the capillary channel. The critical wedge angle at which the liquid pressure turns negative can be evaluated from Eq. 15. Notably, the critical wedge angle for the 3D channel presented here is greater than the value of $(\pi/2 - \theta_c)$ evaluated from the 2D model (Man et al. 1998) because the latter neglects the sidewall effects. The maximum magnitude of the pressure barrier is referred to as the burst pressure. It can be seen from Fig. 3 that a larger wedge angle results in a larger burst pressure. The burst pressures

$$p = - \left(\frac{\partial U_T}{\partial x_{cL}} \right) \left(\frac{\partial V_l}{\partial x_{cL}} \right)^{-1}$$

$$= \left\{ \begin{aligned} & \frac{-2\gamma_{la} \cos \theta_c}{w} \left[\frac{1}{\cos \beta} + \frac{w}{h} + \frac{2x_{cL}}{h} \tan \beta - \frac{\tan \beta}{\sin \alpha_w} \left(\frac{w}{h} + \frac{2x_{cL}}{h} \tan \beta \right) \left(\frac{\alpha_w}{\sin \alpha_w} - \cos \alpha_w \right) \right] \\ & + \frac{2\gamma_{la} \alpha_w \alpha_h \tan \beta}{w \sin \alpha_w \sin \alpha_h} \end{aligned} \right\}$$

$$\times \left[1 + \frac{2x_{cL}}{w} \tan \beta - \frac{\tan \beta}{\sin \alpha_w} \left(1 + \frac{2x_{cL}}{w} \tan \beta \right) \left(\frac{\alpha_w}{\sin \alpha_w} - \cos \alpha_w \right) - \frac{h}{2w \sin \alpha_w \sin \alpha_h} \left(\frac{\alpha_h}{\sin \alpha_h} - \cos \alpha_h \right) \right]^{-1}$$
(18)

are 0.265 and 0.290 kPa for $\beta = 90^\circ$ and 100° , respectively. Moreover, the present 3D model can be extended to take account of the non-uniform interface properties resulted from the use of different materials for channel structures as those reported by Melin et al. (2004) and Chen et al. (2006).

2.2 Burst pressure

Design of capillary-burst valve is based on the burst pressure that depends on the valve geometry and channel–liquid–air interfacial properties. The burst pressure for the 3D model can be obtained either from the pressure expressions given in the transition or expansion regimes. When the liquid pressure turns negative in the transition regime, the meniscus will continue to change shape only by external forcing. As the external forcing is large enough, it propels the liquid to overcome the pressure barrier of the valve, causing the liquid to burst into the divergent section. The burst pressure can be computed from Eq. 15 by taking $\alpha_w = \pi/2 - \theta_c - \beta$, at which α_w reaches its negative maximum in the transition regime. The maximum magnitude of pressure barrier then yields a very simple form as

$$\Delta p_b = \frac{2\gamma_{la}}{w} \left[-\frac{w}{h} \cos \theta_c - \cos(\theta_c + \beta) \right] \quad (19)$$

where the first term in the bracket on the right represents the liquid pressure contributed by the unchanged depth as in Eq. 9, and the second term represents the pressure required to wet the expanded volume beyond the edge as the term b in Eq. 3 proposed by Duffy et al. (1999).

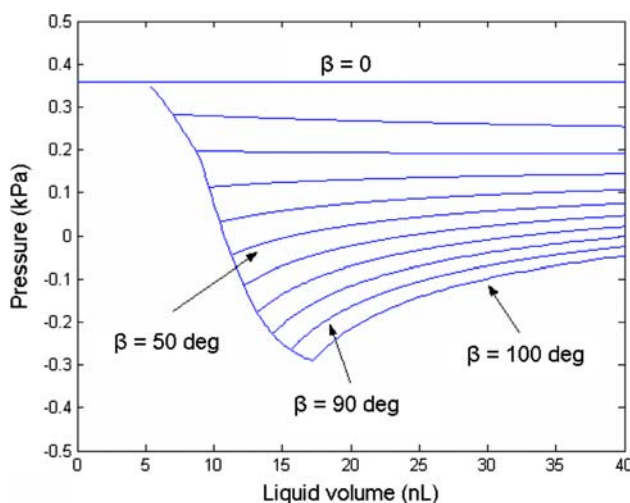


Fig. 3 Variation of liquid pressure with liquid volume for a square channel ($w = h = 300 \mu\text{m}$) with wedge angles ranging from $\beta = 0^\circ$ – 100° . Interfacial properties $\gamma_{la} = 0.072 \text{ N/m}$ and $\theta_c = 68^\circ$ were used for the calculations

The burst pressure may also be evaluated from Eq. 18 in the expansion regime by taking $x_{cL} = 0$ and $\alpha_h = 0$:

$$\Delta p_b = \frac{2\gamma_{la}}{w} \left[-\frac{w}{h} \cos \theta_c + \frac{\cos \theta_c - \frac{\alpha_w \sin \beta}{\sin \alpha_w}}{-\cos \beta + \frac{\sin \beta}{\sin \alpha_w} \left(\frac{\alpha_w}{\sin \alpha_w} - \cos \alpha_w \right)} \right] \quad (20)$$

As the aspect ratio becomes infinite ($w/h = 0$), Eq. 18 will reduce to the 2D result of Man et al. (1998). Note that there should be a “–” sign placed in front the term $\cos \beta$ in the denominator of their Eq. 13. Also note that Eq. 20 can be further reduced to a simpler form exactly identical to Eq. 19 by substituting $(\pi/2 - \theta_c - \beta)$ for α_w .

Moreover, the burst pressure of Eq. 19 is essentially identical to the result derived by Cho et al. (2007). The unique difference is the 3D structure analysis provided in the present study. In their result, the equilibrium contact angle θ_c is replaced by the advancing contact angle θ_A and the term $(\theta_c + \beta)$ in Eq. 19 is modified by substituting an angle defined as $\min\{\theta_A + \beta, 180^\circ\}$ because 180° is the maximum contact angle that a liquid can attain. Based on the modified theory for burst pressure Δp_{mb} ,

$$\Delta p_{mb} = \frac{2\gamma_{la}}{w} \left[-\frac{w}{h} \cos \theta_A - \cos(\min\{\theta_A + \beta, 180^\circ\}) \right] \quad (21)$$

Cho et al. (2007) show that the capillary valve can also work for a hydrophobic channel. When involving a liquid plug in the channel, the receding contact angle θ_R at the rear liquid front may have to be considered in Eq. 21.

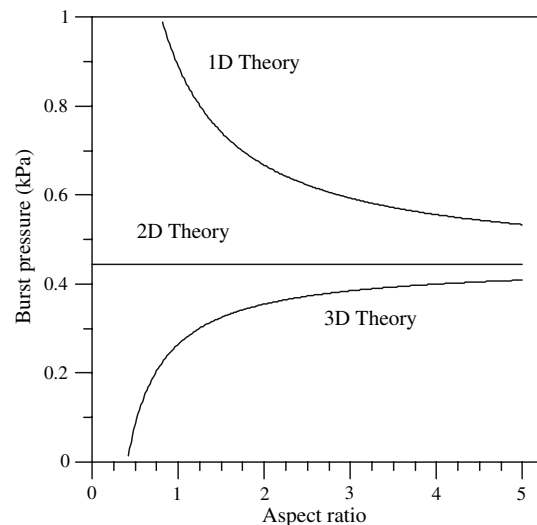


Fig. 4 Comparison of calculated burst pressures based on the 1D, 2D and 3D models for rectangular channels of various aspect ratios with fixed width $w = 300 \mu\text{m}$ and wedge angle $\beta = 90^\circ$. Interfacial properties $\gamma_{la} = 0.072 \text{ N/m}$ and $\theta_c = 68^\circ$ were used for the calculations

Figure 4 compares burst pressures calculated from the 1D, 2D and 3D models for a rectangular channel of various aspect ratios. In the figure, the 1D results are obtained from Eq. 2, the 2D results are computed from the theory derived by Man et al. (1998) for the channels with a fixed width, and the 3D results are given by Eq. 19. The 1D theory that assumes sudden expansions in both of the width and depth directions as in the axisymmetric case predicts a rather higher burst pressure for small aspect ratios ($h/w \ll 1$). The predicted value is then followed by a rapid decrease with increasing aspect ratio becoming closer to the 2D theory. At an infinitely large aspect ratio, $D_h = 2w$ and the 1D theory yields $\Delta p_b = 2\gamma_{la}\sin\theta_c/w$, which is exactly the value of 0.445 kPa calculated from the 2D theory. The present theory based on the 3D model obviously gives a more reasonable prediction. The capillary valve becomes effective at an aspect ratio of $h/w = 0.4$ and then the burst pressure increases with the aspect ratio until it approaches the 2D value at a large aspect ratio as one can expect from Eq. 20. Note that the burst pressure can be converted into the corresponding burst rotational speed for capillary-burst valves fabricated on a rotating disk.

3 Experimental setup

The experiments were carried out using the image-capturing unit in synchronization with the rotational motion. Figure 5 illustrates the schematic arrangement of the coupled optic-rotation apparatus. The centrifugal pumping was achieved by employing a DC motor (AS46AA, Oriental Motor) to drive the disk in which the microfluidics as depicted in Fig. 1 was microstructured. The reservoir of 8 mm in diameter is located at $r_1 = 27$ mm and the capillary valve is at $r_2 = 31.5$ mm for the present experiments. The accuracy of the rotational speeds (100–1,000 rpm)

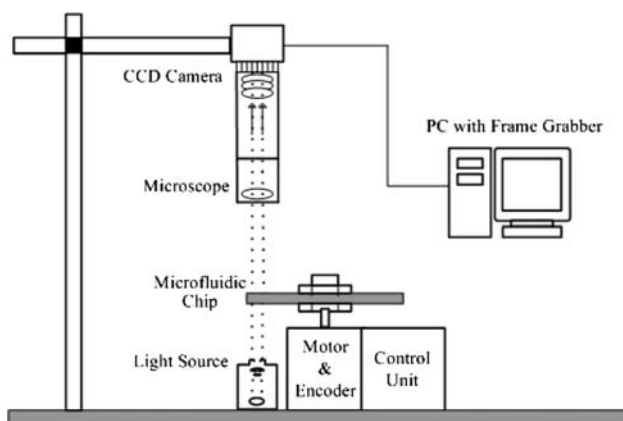


Fig. 5 Experimental arrangement for flow visualization of microfluidics on a rotating disk

tested in the present study was within $\pm 0.2\%$. The angular position of the microchannel on the disk was acquired and controlled through an optical encoder (10,000 pulse/rev). The signals from the encoder were used to synchronize the image-capturing unit. The image unit consisted of a frame grabber (Metro-II/CL, Matrox) and a CCD camera (CV-M71CL, 768×576 pixels, JAI) in conjunction with a microscope ($2\times$ or $10\times$ objective, Mitsutoyo) above the disk to obtain flow images. The $2\times$ microscope lens has a depth of focus of $91 \mu\text{m}$ and a resolution of $5 \mu\text{m}$. The $10\times$ lens has a depth of focus of $3.5 \mu\text{m}$ and a resolution of $1 \mu\text{m}$. A halogen lamp (MHF-M1001, Moritex) served for illumination beneath the disk. In synchronization with the rotational motion, the CCD camera having a maximum frame rate of 60 fr/s can be triggered to allow one shot of the targeted object on the rotating disk per revolution.

The microfluidic structures were machined using a micro-CNC in a PMMA (polymethylmethacrylate) disk of 10 cm in diameter and 2 mm thick. The microstructured disk was then bonded with another PMMA disk on a hot plate at a temperature of 63°C and a pressure of $65\text{--}70 \text{ kgf/cm}^2$ for 20 min. All of the centrifugal-based microfluidic disks were machined having a channel width of 300 or 400 μm with various depths (80–600 μm) and wedge angles ($30^\circ\text{--}100^\circ$). The fluid used in the experiments was de-ionized water. For clear visualization, the de-ionized water was mixed with a small amount of red ink. The contact angle between the fluid and the PMMA surface was measured using a dynamic contact angle system (FTÅ200, First Ten Angstroms) at $68^\circ \pm 1^\circ$.

4 Results and discussion

The synchronized image-capturing system developed in the present study enables us to visualize the liquid flow that bursts out at the capillary valve to fill the expanded volume as the rotational speed exceeds the threshold value. Figure 6 shows flow visualization images of the liquid blocked by the capillary valve with $\beta = 60^\circ$ and channel cross-section of $w = h = 300 \mu\text{m}$ on a stationary disk. The meniscus, which can be more clearly seen in the picture taken with the $10\times$ objective, is nearly flat at the valve edge ($x_c = L$) for the stationary case. As the disk rotates at a low speed $\Omega = 240$ rpm, it can be seen in Fig. 7 that the liquid still stops at the valve edge with its meniscus curving outward to balance the centrifugal force. Figure 8 displays sequential images of the liquid flow that bursts into the valve as the speed is increased to 300 rpm higher than the predicted burst value of 260 rpm. Note that the black line on the meniscus contour is conjectured a result of inclined and curved meniscus surface across the channel depth. The sequential images show that the liquid enters the expanded

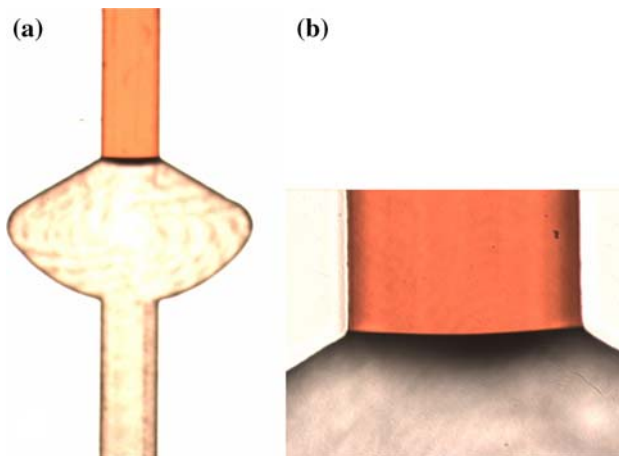


Fig. 6 Liquid front stops at the sudden opening of the capillary valve ($w = h = 300 \mu\text{m}$ and $\beta = 60^\circ$) on a resting disk. The left picture (a) was taken using $\times 2$ objective (resolution $5 \mu\text{m}$) and the right one (b) using $\times 10$ objective (resolution $1 \mu\text{m}$) focusing at the meniscus

volume at a slow flow rate taking 3.2 s for the meniscus to advance to halfway in the divergent section. Then, a quick flooding ($t = 3.2\text{--}3.4 \text{ s}$) occurs and the liquid fills the whole valve. The liquid gradually occupies the divergent section with a liquid front of convex shape but having a hydrophilic contact angle (less than 90°) with the side walls. The “effective” contact angles with the side walls may be estimated from the images that are applicable. It is found that the “effective” contact angle varies from $60^\circ \pm 2^\circ$ at $t = 0.2\text{--}0.4 \text{ s}$, to $65^\circ \pm 3^\circ$ at $t = 0.6\text{--}1.6 \text{ s}$, then $70^\circ \pm 3^\circ$ at $t = 1.8\text{--}3.0 \text{ s}$, and finally rises rapidly to $86^\circ \pm 2^\circ$ at $t = 3.2 \text{ s}$. During the early development



Fig. 7 Liquid front stops at the sudden opening of the capillary valve ($w = h = 300 \mu\text{m}$ and $\beta = 60^\circ$) on a rotating disk at a speed of 240 rpm

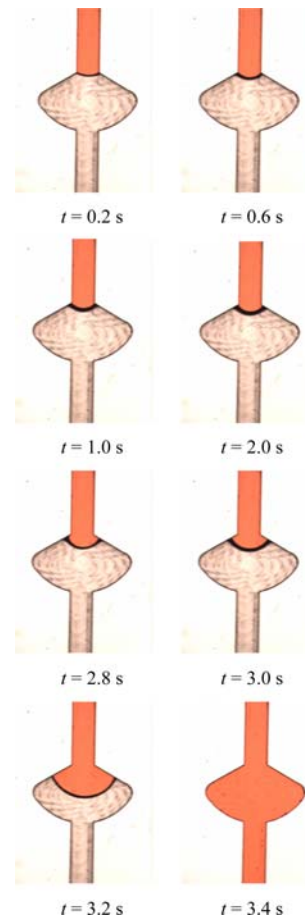


Fig. 8 Sequential images of the liquid flow burst into the capillary valve ($w = h = 300 \mu\text{m}$ and $\beta = 60^\circ$) at a rotational speed of 300 rpm for the time $t = 0.2\text{--}3.4 \text{ s}$

($t = 0.6\text{--}3.0 \text{ s}$) of the meniscus in the expansion regime, the measured “effective” contact angle is in accordance with the assumption ($\theta_{\text{eff}} = \theta_c = \pi/2 - \alpha_w - \beta$) made to derive the burst pressure of Eqs. 19, and 20. As the meniscus reaches halfway in the divergent section at $t = 3.2 \text{ s}$, where the quick flooding occurs and momentum effects become significant, the dynamic contact angle may have to be considered in the analytical modeling. Moreover, the meniscus movement during $t = 2.0\text{--}3.2 \text{ s}$ in Fig. 8 appears to retain its shape, which is consistent with the derivation leading to Eq. 18 where only the change in x_{cL} (the marching distance along the channel axis in the divergent section) is considered for the variation.

The burst conditions for various capillary channel dimensions were carefully measured by comparing the rotational speed and the microscopic image of the flow. For each of the data points presented, the burst rotational speed was repeatedly examined at least three times. The uncertainty of the burst rotational speeds presented in the following figures is approximately within $\pm 4\%$. Figure 9 compares the measured burst rotational speeds with the 3D

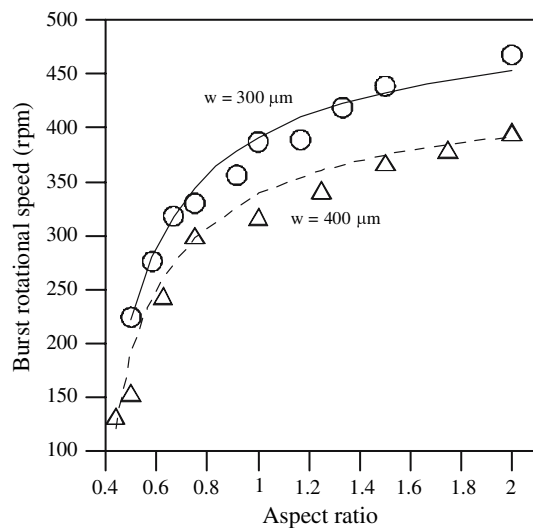


Fig. 9 Comparison of the predicted burst rotational speeds from the 3D theory ($\gamma_{la} = 0.072$ N/m, $\theta_c = 68^\circ$, solid line for $w = 300$ μm and dashed line for $w = 400$ μm) with the measurements for the channels of $w = 300$ μm (circle) and 400 μm (triangle) with various aspect ratios ($h/w = 0.42$ – 2.0). The uncertainty of the measured burst rotational speeds is approximately $\pm 4\%$

theory of Eq. 19 for capillary valves with channel cross-sections of various aspect ratios while the wedge angle is fixed at $\beta = 90^\circ$. Both the theory and experiment show that the burst rotational speed is higher for the valve with smaller channel width and larger aspect ratio. The 3D theory agrees well with the measurements, in which even the largest deviations are found to be less than 6%. Figure 10 shows a similar comparison for the variation with wedge angles ($\beta = 50^\circ$ – 100°) for square channels. Note that the wedge angle was purposely widened over 90° to examine the validity of the theory. The capillary valve becomes effective at $\beta = 50^\circ$ as predicted by the theory. The agreement on burst rotational speed between the theory and experiment is good particularly for the valves with a smaller channel width ($w = 300$ μm) including the case of $\beta = 100^\circ$. For the valves with a larger channel width ($w = 400$ μm), the measured speeds are generally lower than the prediction yielding a deviation in the range of 6–10% for $\beta = 80^\circ$ – 100° . This may be partly due to uncertainties on geometry and surface quality and partly due to the fact that the liquid momentum is considered negligible throughout the entire derivation to obtain the pressure.

The roughness of the machined channel surface was measured using a stylus profilometry (SE3500K, Kosaka Lab) at 1.4 – 2.4 μm Ra. How the surface roughness affects the burst pressure may be understood from its effect on contact angle as were discussed by a number of studies (Wenzel 1936; Lambert et al. 2003; Katoh 2004). These studies generally suggest that the contact angle of a smooth surface is decreased by roughness for a hydrophilic surface

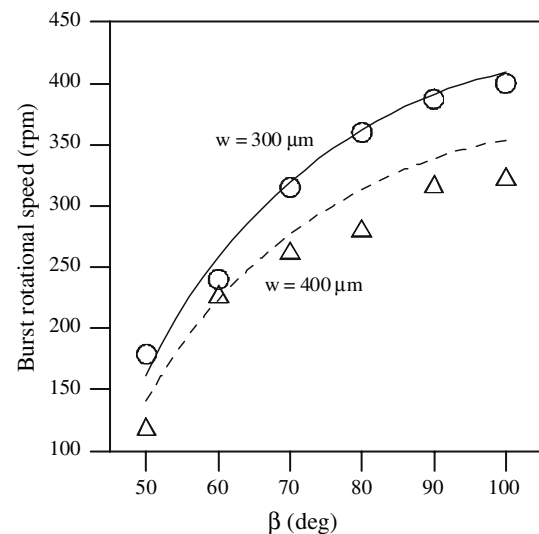


Fig. 10 Comparison of the predicted burst rotational speeds from the 3D theory ($\gamma_{la} = 0.072$ N/m, $\theta_c = 68^\circ$, solid line for $w = 300$ μm and dashed line for $w = 400$ μm) with the measurements for the square channels of $w = h = 300$ μm (circle) and 400 μm (triangle) with various wedge angles ($\beta = 50^\circ$ – 100°). The uncertainty of the measured burst rotational speeds is approximately $\pm 4\%$

and increased for a hydrophobic surface. In other words, roughness makes hydrophilic surface more hydrophilic and hydrophobic surface more hydrophobic. When examining the effect of roughness on Eq. 19, one discovers that roughness tends to cause a decrease in burst pressure. Quantitatively, a decrease of 3° in θ_c will result in a decrease of 6.4% in the burst rotational speed for a square channel with $\beta = 90^\circ$. However, the dependence of burst pressure on contact angle could be much more complicated than such a simple argument. Considering the meniscus is in motion, Cho et al. (2007) suggest the use of advancing contact angle θ_A instead of the equilibrium contact angle θ_c for computing the burst pressure from Eq. 19. As a result, the burst pressure computed using θ_A is greater than that using θ_c because $\theta_A > \theta_c$. Therefore, the surface roughness and the associated contact angle could have a mixed impact on the burst pressure.

The effect of momentum on the burst pressure was previously addressed by Zeng et al. (2000) in terms of a fluidic capacitance that takes into account of the energy loss due to meniscus oscillation and viscous dissipation. Alternatively, the momentum effect may be evaluated based on the average velocity of the liquid flow in the channel. For the channel with $w = h = 400$ μm and $\beta = 80^\circ$, which yields the worst deviation of 10%, an average velocity $u_o = 0.13$ m/s was estimated for $\Omega = 300$ rpm from the time needed to empty the reservoir. The velocity in this case could contribute as much as 17 N/m² in momentum difference (ρu_o^2) across the capillary valve corresponding to a deviation of 5.5% below the

predicted burst rotational speed (310 rpm). It should be noted that the average velocity of laminar flow in a centrifugal-based channel is approximated to be proportional to the cross-sectional area and to the square of rotational speed (Ducrée et al. 2006). On the other hand, the burst pressure (or the square of the burst rotational speed) predicted from Eq. 19 appears to be inversely proportional to the channel dimension. Accordingly, the momentum effect on the burst pressure is expected to diminish rapidly as the channel dimensions become smaller. Further studies need to clarify the actual role of momentum in a capillary valve as well as the details of the effects due to surface quality and the associated contact angle variation.

In the present experiments, the measurements of burst pressure were carried out for channels having widths of 300 and 400 μm . In the range of smaller dimensions, Cho et al. (2007) have made similar measurements for centrifugal microchannels of widths $w = 15\text{--}150\text{ }\mu\text{m}$ with fixed $h = 150\text{ }\mu\text{m}$ and found reasonable agreement between the measured burst rotational speeds and the modified theory of Eq. 21, which considers the advancing and receding contact angles for the liquid plug in the experiments of Cho et al. (2007). However, for very narrow channels ($w < 40\text{ }\mu\text{m}$) the measured data are noticeably lower than the theoretical results, indicating the increasing sensitivity of the burst rotational speed to the channel geometry of small sizes. In general, the measured burst rotational speeds in the smaller dimension range ($w = 36\text{--}150\text{ }\mu\text{m}$) scale as $\sim(1/w)^m$ with $m \approx 0.4$, slightly less than the one-half power approximated by the present 3D theory.

5 Conclusions

An analytical study has been carried out to investigate the pressure barrier in a capillary-burst valve with a sudden expansion in channel cross-section. The analysis of the internal liquid pressure is based on the surface energy for 3D meniscus shape in a rectangular channel where the sudden expansion is made with a wedge angle in the width direction only. An analytical expression of simple form has been found to predict the burst pressure required for a capillary valve. This simple expression relates the burst pressure to the channel dimensions (w and h) and the valve geometry (β) as well as the surface property (γ_{la} and θ_{c}). The burst pressure derived from the 3D model will reduce to the 2D analytical expression of Man et al. (1998) when assuming a channel depth much greater than its width. Our expression of burst pressure is also essentially identical to the result derived by Cho et al. (2007). However, the present study provides a more thorough 3D structure analysis. Capillary valves are commonly used to regulate liquid flow in centrifugal microfluidics. Experimental

apparatus was developed for visualization and measurements of the liquid flow in the CD-based microfluidics equipped with a capillary valve. The microfluidics was machined in a PMMA disk and sandwiched with another PMMA disk. The visualization images clearly show the development of the meniscus shape during the burst of the liquid from the capillary channel into the expanded volume. The meniscus development observed in the experiments also supports the assumptions made in the present analysis for the derivation of pressure barrier in a capillary valve. Both the theory and the experiment consistently show that the burst rotational speed is higher for the valve with a smaller channel width, larger aspect (depth-to-width) ratio and wider wedge angle. The 3D theory is in good agreement with the measurements of burst rotational speed particularly for the valves with a smaller channel width ($w = 300\text{ }\mu\text{m}$). For the valves with a channel of larger square cross-section ($w = h = 400\text{ }\mu\text{m}$), the measured rotational speeds are found to be significantly lower than the predictions by nearly 10% for those with larger wedge angles ($\beta = 80^\circ\text{--}100^\circ$) which require relatively higher burst values (310–350 rpm) than those with smaller wedge angles. This discrepancy may be attributed to the surface quality and the associated contact angle variation as well as the neglect of liquid momentum in the derivation leading to the present 3D theory. Nevertheless, the present 3D theory is shown to be more accurate than previous 1D and 2D theories in evaluating the burst pressure for capillary valves. The simple expression of burst pressure derived here provides a convenient tool for design of capillary valves.

Acknowledgments The authors are grateful for the financial support for this study from National Science Council of Taiwan under Contract Number NSC 94-2212-E-005-017.

References

- Auroux P-A, Iossifidis D, Reyes DR, Manz A (2002) Micro total analysis systems. 2. Analytical standard operations and applications. *Anal Chem* 74:2637–2652
- Chen JM, Lin M-G, Huang P-C (2006) Design of capillary valves for microfluidics on a rotating disk. In: Proceedings of 2nd international symposium on micro and nano technology, ISM-NT-2, Hsinchu, pp 100–103
- Cho H, Kim H-Y, Kang JY, Kim TS (2007) How the capillary microvalve works. *J Colloid Interface Sci* 306:379–385
- Ducrée J, Haeberle S, Brenner T, Glatzel T, Zengerle R (2006) Patterning of flow and mixing in rotating radial microchannels. *Microfluid Nanofluid* 2:97–105
- Duffy DC, Gillis HL, Lin J, Sheppard NF Jr, Kellogg GJ (1999) Microfabricated centrifugal microfluidic systems: characterization and multiple enzymatic assays. *Anal Chem* 71:4669–4678
- Glière A, Delattre C (2006) Modeling and fabrication of capillary stop valves for planar microfluidic systems. *Sens Actuators A* 130–131:601–608

- Grumann M, Geipel A, Riegger L, Zengerle R, Ducrée J (2005) Batch-mode mixing on centrifugal microfluidic platforms. *Lab Chip* 5:560–565
- Gustafsson M, Hirschberg D, Palmberg C, Jörnvall H, Bergman T (2004) Integrated sample preparation and MALDI mass spectrometry on a microfluidic compact disk. *Anal Chem* 76:345–350
- Haeblerle S, Brenner T, Zengerle R, Ducrée J (2006) Centrifugal extraction of plasma from whole blood on a rotating disk. *Lab Chip* 6:776–781
- Kato K (2004) Measurement of contact angle and surface tension. In: Hartland S (ed) *Surface and interfacial tension: measurement, theory and applications*. Dekker, New York, pp 375–546
- Kim DS, Lee K-C, Kwon TH, Lee SS (2002) Micro-channel filling flow considering surface tension effect. *J Micromech Microeng* 12:236–246
- Kim E, Whitesides GM (1997) Imbibition and flow of wetting liquids in noncircular capillary. *J Phys Chem B* 101:855–863
- Lambert P, Pierre Letier P, Delchambre A (2003) Capillary and surface tension forces in the manipulation of small parts. In: *Proceedings of the 5th IEEE international symposium on assembly and tasks planning (ISATP)*, Besançon, pp 54–59
- Lee J, Moon H, Fowler J, Schoellhammer T, Kim C-J (2002) Electrowetting and electrowetting-on-dielectric for microscale liquid handling. *Sens Actuators A* 95:259–268
- Leu T-S, Chang P-Y (2004) Pressure barrier of capillary stop valves in micro sample separators. *Sens Actuators A* 115:508–515
- Madou M, Zoval J, Jia G, Kido H, Kim J, Kim N (2006) Lab on a CD. *Annu Rev Biomed Eng* 8:601–628
- Madou MJ, Lee LJ, Daunert S, Lai S, Shih C-H (2001a) Design and fabrication of CD-like microfluidic platforms for diagnostics: microfluidic functions. *Biomed Microdevices* 3:245–254
- Madou MJ, Lu Y, Lai S, Koh CG, Lee LJ, Wenner BR (2001b) A novel design on a CD disc for 2-point calibration measurement. *Sens Actuators A* 91:301–306
- Man PF, Mastrangelo CH, Burns MA, Burke DT (1998) Microfabricated capillary-driven stop valve and sample injector. In: *Proceedings of 11th annual international workshop on micro electro mechanical systems*, Heidelberg, pp 45–50
- Manz A, Grabber N, Widmer HM (1990) Miniaturized total chemical analysis systems: a novel concept for chemical sensing. *Sens Actuators B* 1:244–248
- McNeely MR, Spute MK, Tusneem NA, Oliphant AR (1999) Hydrophobic microfluidics. In: Ahn CH, Frazier AB (eds) *Proceedings of SPIE—microfluidic devices & systems II*, vol. 3877, pp 210–220
- Melin J, Roxhed N, Gimenez G, Griss P, van der Wijngaart W, Stemme G (2004) A liquid-triggered liquid microvalve for on-chip flow control. *Sens Actuators B* 100:463–468
- Nguyen N-T, Huang X (2005) Thermocapillary effect of a liquid plug in transient temperature fields. *Jpn J Appl Phys* 44:1139–1142
- Nguyen N-T, Wereley ST (2002) *Fundamentals and applications of microfluidics*. Artech House, Boston
- Oh KW, Ahn CH (2006) Topical review: a review of microvalves. *J Micromech Microeng* 16:R13–R39
- Reyes DR, Iossifidis D, Auroux P-A, Manz A (2002) Micro total analysis systems 1. Introduction, theory, and technology. *Anal Chem* 74:2623–2636
- Wenzel RN (1936) Resistance of solid surfaces to wetting by water. *Indust Eng Chem* 28:988–994
- Zeng J, Deshpande M, Greiner KB, Gilbert JR (2000) Fluidic capacitance model of capillary-driven stop valve. In: *MEMS proceedings of ASME international mechanical engineering congress and exposition*, Orlando